



## Probing the chemistry of adhesion between a 316L substrate and spin-on-glass coating

Lampert, Felix; Kadkhodazadeh, Shima; Kasama, Takeshi; Dahl, Kristian Vinter; Christiansen, Alexander Bruun; Møller, Per

*Published in:*  
Langmuir

*Link to article, DOI:*  
[10.1021/acs.langmuir.7b03131](https://doi.org/10.1021/acs.langmuir.7b03131)

*Publication date:*  
2018

*Document Version*  
Peer reviewed version

[Link back to DTU Orbit](#)

### *Citation (APA):*

Lampert, F., Kadkhodazadeh, S., Kasama, T., Dahl, K. V., Christiansen, A. B., & Møller, P. (2018). Probing the chemistry of adhesion between a 316L substrate and spin-on-glass coating. *Langmuir*, 34(10), 3170-3176. <https://doi.org/10.1021/acs.langmuir.7b03131>

---

### General rights

Copyright and moral rights for the publications made accessible in the public portal are retained by the authors and/or other copyright owners and it is a condition of accessing publications that users recognise and abide by the legal requirements associated with these rights.

- Users may download and print one copy of any publication from the public portal for the purpose of private study or research.
- You may not further distribute the material or use it for any profit-making activity or commercial gain
- You may freely distribute the URL identifying the publication in the public portal

If you believe that this document breaches copyright please contact us providing details, and we will remove access to the work immediately and investigate your claim.

## Probing the chemistry of adhesion between a 316L substrate and spin-on-glass coating

Felix Lampert, Shima Kadkhodazadeh, Takeshi Kasama, Kristian Vinter Dahl, Alexander Bruun Christiansen, and Per Møller

*Langmuir*, **Just Accepted Manuscript** • DOI: 10.1021/acs.langmuir.7b03131 • Publication Date (Web): 19 Feb 2018

Downloaded from <http://pubs.acs.org> on February 21, 2018

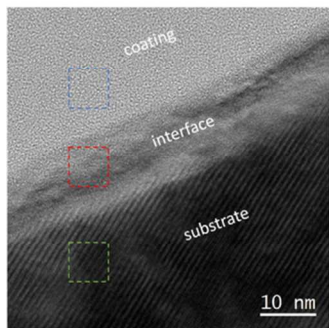
### Just Accepted

“Just Accepted” manuscripts have been peer-reviewed and accepted for publication. They are posted online prior to technical editing, formatting for publication and author proofing. The American Chemical Society provides “Just Accepted” as a service to the research community to expedite the dissemination of scientific material as soon as possible after acceptance. “Just Accepted” manuscripts appear in full in PDF format accompanied by an HTML abstract. “Just Accepted” manuscripts have been fully peer reviewed, but should not be considered the official version of record. They are citable by the Digital Object Identifier (DOI®). “Just Accepted” is an optional service offered to authors. Therefore, the “Just Accepted” Web site may not include all articles that will be published in the journal. After a manuscript is technically edited and formatted, it will be removed from the “Just Accepted” Web site and published as an ASAP article. Note that technical editing may introduce minor changes to the manuscript text and/or graphics which could affect content, and all legal disclaimers and ethical guidelines that apply to the journal pertain. ACS cannot be held responsible for errors or consequences arising from the use of information contained in these “Just Accepted” manuscripts.

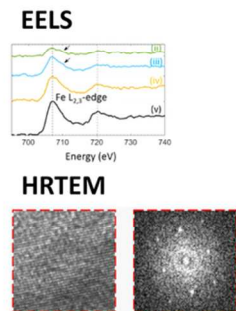


1  
2  
3  
4  
5  
6  
7  
8  
9  
10  
11  
12  
13  
14  
15  
16  
17  
18  
19  
20  
21  
22  
23  
24  
25  
26  
27  
28  
29  
30  
31  
32  
33  
34  
35  
36  
37  
38  
39  
40  
41  
42  
43  
44  
45  
46  
47  
48  
49  
50  
51  
52  
53  
54  
55  
56  
57  
58  
59  
60

**Investigation of bonding  
in SOG/substrate interface**



**Characterization by  
TEM**



**Discussion of bonding  
mechanism**

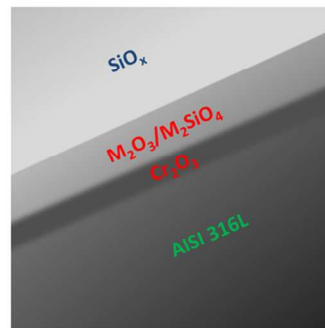


Table of Contents/Abstract Graphic

87x38mm (300 x 300 DPI)

# Probing the chemistry of adhesion between a 316L substrate and spin-on-glass coating

Felix Lampert<sup>a</sup>, Shima Kadkhodazadeh<sup>b</sup>, Takeshi Kasama<sup>b</sup>, Kristian Vinter Dahl<sup>a</sup>, Alexander Bruun Christiansen<sup>c</sup>, Per Møller<sup>a</sup>

<sup>a</sup> Technical University of Denmark, Department of Mechanical Engineering, Produktionstorvet 425, 2800 Kgs. Lyngby, Denmark

<sup>b</sup> Technical University of Denmark, Center for Electron Nanoscopy (CEN), Fysikvej 307, 2800 Kgs. Lyngby, Denmark

<sup>c</sup> SiOx ApS, Bybjergvej 7, 3600 Espergærde, Denmark

## Abstract

Hydrogen silsesquioxane ( $[\text{HSiO}_{3/2}]_n$ ) based “spin-on-glass” has been deposited on 316L substrate and cured in Ar/H<sub>2</sub> gas atmosphere at 600 °C to form a continuous surface coating with sub-micrometer thickness. The coating functionality depends primarily on the adhesion to the substrate, which is largely affected by the chemical interaction at the interface between the coating and the substrate. We have investigated this interface by transmission electron microscopy and electron energy loss spectroscopy. The analysis identified a 5-10 nm thick interaction zone containing signals from O, Si, Cr and Fe. Analysis of the energy loss near edge structure of the present elements identified predominantly signal from  $[\text{SiO}_4]^{4-}$  units together with  $\text{Fe}^{2+}$ ,  $\text{Cr}^{2+}$  and traces of  $\text{Cr}^{3+}$ . High-resolution transmission electron microscopy images of the interface region confirm a crystalline  $\text{Fe}_2\text{SiO}_4$  interfacial region. In agreement with computational thermodynamics, it is proposed that the spin-on-glass forms a chemically bonded silicate-rich interaction zone with the substrate. It was further suggested that this zone is composed of a corundum-type oxide at the substrate surface, followed by an olivine-

1  
2  
3 structure intermediate phase and a spinel-type oxide in the outer regions of the interfacial  
4  
5 zone.  
6  
7

## 9 **1 Introduction**

11 Due to their inherent resistance towards galvanic corrosion combined with good formability,  
12  
13 austenitic stainless steels belong to the most widely used engineering materials. Apart from  
14  
15 the chemical composition and the mechanical/thermal history, the functionality of the  
16  
17 materials is greatly determined by the surface finish, and hence their surface modification  
18  
19 plays a major role in the development of improved stainless steel engineering components.  
20  
21 Over the recent years, intense research effort has been directed into the surface modification  
22  
23 by SiO<sub>x</sub>-based micrometer/sub-micrometer thick coatings to improve the wear resistance<sup>1,2</sup>,  
24  
25 biocompatibility<sup>3,4</sup>, bio fouling characteristics and cleanability<sup>5,6</sup>, surface morphology<sup>7-10</sup> and  
26  
27 corrosion resistance in saline<sup>11-13</sup>, acid<sup>11,14,15</sup> or high temperature<sup>16</sup> environments of stainless  
28  
29 steel components at a minimal impact on the component geometry. Apart from the traditional  
30  
31 deposition processes, such as chemical vapor deposition<sup>17</sup>, physical vapor deposition<sup>18</sup>, sol-gel  
32  
33 processing<sup>19</sup> or liquid phase deposition<sup>20</sup>, the deposition from hydrogen silsesquioxane  
34  
35 (HSQ), [HSiO<sub>3/2</sub>]<sub>n</sub>, spin-on-glass (SOG) has shown excellent results for the processing of high  
36  
37 quality SiO<sub>x</sub>-like thin films<sup>21,22</sup>. In addition to the deposition of near stoichiometric silica  
38  
39 films, SOG-technology offers the possibility to deposit fully inorganic films with various  
40  
41 degrees hydrogenation as intermediate reaction products, resulting in a broad range of film  
42  
43 properties<sup>21-23</sup>. While the material was mainly developed for microelectronics applications<sup>23,24</sup>  
44  
45 or as electron beam resist<sup>25</sup>, it has recently emerged into the surface finishing industry and  
46  
47 shown an outstanding performance as coating material for metallic substrates such as  
48  
49 aluminum or tool steel<sup>7-10</sup>.  
50  
51  
52  
53  
54  
55  
56  
57  
58  
59  
60

1  
2  
3 Recently, we have shown the applicability of SOG as material for sub-micrometer thick  
4 coatings on stainless steel substrates<sup>26–28</sup>. Our studies have proven the concept of precursor  
5 deposition by an industrially applicable dip-coating process and the subsequent coating curing  
6 in both oxidizing<sup>27,28</sup> and non-oxidizing<sup>26</sup> atmosphere, showing that both processes may yield  
7 well adherent coatings with 200-400 nm thickness on substrates with 2B finish<sup>29</sup>; however,  
8 we have also demonstrated that the coating efficiently levels the substrate surface, and thus  
9 fills substrate defects (e.g. surface voids), which may consequently lead to a local increase in  
10 coating thickness exceeding 1400 nm<sup>26</sup>. Further, we have shown that oxidative curing induces  
11 thermal oxidation of the substrate<sup>27</sup>, leading to adhesive failure of the coating and ultimately  
12 to functional component failure<sup>28</sup>. We have reported that the formation of a thick, detrimental  
13 interface was driven by an abundance of oxygen in the curing atmosphere<sup>27</sup>, and that the  
14 formation of a thick interfacial zone can be suppressed by a removal of oxygen from the  
15 curing atmosphere, i.e. by curing in a non-oxidizing atmosphere such as Formiergas<sup>26</sup>.  
16 However, the methods applied in the previous work were inadequate to clearly resolve the  
17 interface between the coating and the substrate and, hence, the interfacial chemistry,  
18 morphology and the bonding mechanism between coating and substrate are unclear.  
19

20  
21  
22 In agreement with other studies<sup>11,13,30–35</sup>, our previous findings<sup>27,28</sup> emphasize the significance  
23 of the coating/substrate interface for both the adhesion and the performance of glass coatings  
24 on stainless steel. However, to the author's knowledge, previous studies have generally  
25 focused on the formation of thick interface oxides<sup>31–33</sup>, traditional enameling technology of  
26 complex industrial porcelains<sup>30</sup> or on vapor deposition techniques<sup>34,35</sup>, which may lead to  
27 significantly different bonding mechanisms. Consequently, the interface formation of well  
28 adherent, non-oxidatively cured HSQ-based coatings cannot be adequately deduced based on  
29 previous literature. Hence, the present study aims at a detailed characterization of the  
30 interfacial chemistry of non-oxidatively cured SOG on type 316L substrate by Transmission  
31  
32  
33  
34  
35  
36  
37  
38  
39  
40  
41  
42  
43  
44  
45  
46  
47  
48  
49  
50  
51  
52  
53  
54  
55  
56  
57  
58  
59  
60

1  
2  
3 Electron Microscopy (TEM). The interface was characterized by electron energy loss  
4 spectroscopy in scanning-TEM together with and high resolution TEM and the analytical  
5 results are discussed based on the thermodynamical oxide/metal phase equilibrium at the  
6 interface. This analysis provides novel insights into the metal-glass bonding mechanism of  
7 silica-like coatings on stainless steel substrate and, in conclusion, the adhesive performance of  
8 the coatings.  
9  
10  
11  
12  
13  
14  
15  
16  
17

## 18 **2 Experimental section**

19  
20 To analyze the bonding mechanism between a stainless steel substrate and a SOG coating,  
21 AISI 316L substrates (composition in Table I) with no. 2B surface finish were coated with  
22 HSQ-based SOG by the method previously described in Lampert *et al.*<sup>26</sup>. The test coupons  
23 were dip coated in commercial HSQ-solution (Dow Corning FOx 25) and subjected to a two  
24 stage heat treatment, the first step being a soft bake at 160 °C in air and the second a  
25 polymerization at 600 °C under flow of 0.5 l/min Ar/H<sub>2</sub> gas mixture (10 vol.% H<sub>2</sub>) for 2h. The  
26 temperature of the polymerization stage was elevated with respect to our previous work<sup>26</sup> in  
27 order to decrease the susceptibility of the coating material to ionizing irradiation<sup>36</sup> during ion  
28 beam milling and the TEM investigation.  
29  
30  
31  
32  
33  
34  
35  
36  
37  
38  
39

40 Lamellae for TEM investigations were prepared by focused ion beam (FIB) milling in a FEI  
41 Helios NanoLab 600 dual beam scanning electron microscope (SEM). The specimens were  
42 first sputter coated with 20-30 nm of Au to avoid surface charging during the FIB preparation,  
43 followed by in-situ deposition of a Pt layer prior to milling to protect the sample from  
44 irradiation damage. FIB-milling was carried out at 30 kV ion beam accelerating voltage,  
45 followed by final polishing at 2 kV ion beam accelerating voltage and 0.44 nA ion beam  
46 current. The lamellae were additionally polished in a Fischione NanoMill precision Ar-ion  
47 mill (500 V accelerating voltage and 100 pA beam current) to remove the residual FIB  
48  
49  
50  
51  
52  
53  
54  
55  
56  
57

1  
2  
3 damage. The TEM examination of the samples was performed in a FEI Titan 80-300kV  
4  
5 instrument fitted with a FEG electron source, a monochromator and a GIF Tridiem electron  
6  
7 energy loss spectroscopy (EELS) spectrometer. Scanning-TEM (STEM) -EELS  
8  
9 measurements were carried out at 120 kV accelerating voltage. In STEM, spatial resolutions  
10  
11 of 5 Å and 1.5 Å, respectively with and without the monochromator excited, were obtained.  
12  
13 The EELS measurements were acquired with the monochromator excited and had an energy  
14  
15 resolution of 0.15 eV. High-resolution TEM (HRTEM) imaging was carried out at 300 kV  
16  
17 and with the point to point resolution of 1.4 Å. Thermodynamic phase equilibrium  
18  
19 calculations were performed in Thermo-Calc version 2017a<sup>37</sup> using version 7.0 of the  
20  
21 Thermo-Calc Software steel database TCFE. The elements Fe, Cr, Mn, Ni, Si and O were  
22  
23 considered in the calculations.  
24  
25  
26  
27

### 28 **3 Results and Discussion**

29  
30  
31 A high-angle annular dark-field (HAADF) STEM image of the coating – substrate cross-  
32  
33 section is shown in Figure 1(a). Image intensity in HAADF STEM is primarily related to the  
34  
35 atomic number (Z-contrast) of the material, indicating an interfacial region distinct from the  
36  
37 coating and the substrate (labelled “interface”). This is similar to our previous investigation of  
38  
39 an oxidatively cured coating<sup>27</sup>, where an interfacial reaction zone was detected. Here, a much  
40  
41 thinner interfacial zone of 5 – 10 nm is detected, compared to in the oxidatively cured coating.  
42  
43 EELS line scans spanning energy ranges 400 – 1000 eV (covering the O K-edge and Cr, Mn,  
44  
45 Fe and Ni L<sub>2,3</sub>-edges) and 90 – 150 eV (containing the Si L<sub>2,3</sub>-edge) were acquired from the  
46  
47 coating/substrate interface, in order to probe the chemistry of this interfacial zone. The Si L<sub>2,3</sub>-  
48  
49 edge had to be recorded separately, as our experimental setup limits the spectral energy range  
50  
51 to 600 eV at most, and thus we were unable to record all edges of interest together in the same  
52  
53 spectrum. The relative composition profile of O, Cr and Fe calculated from the EEL spectra  
54  
55 along with the HAADF intensity profile and the intensity of the Si signal along a line across  
56  
57  
58  
59  
60



1  
2  
3 the interface are plotted in Figure 1(b). Approximate boundaries for the substrate and the  
4  
5 coating, determined from the changes in the HAADF image intensity profile along the  
6  
7 recorded line scans, are marked in the graphs. We were unable to analyze the composition  
8  
9 profile of Ni, due to the pronounced overlap between the Ni L<sub>2,3</sub>-edge and the Fe L<sub>1</sub>-edge. The  
10  
11 detection of the Mn L<sub>2,3</sub>-edge was also hindered due to its low concentration and low signal  
12  
13 level in the measurements. The measurements were repeated across different regions of the  
14  
15 sample and were found to be reproducible. As evident in the graphs in Figure 1(b) the  
16  
17 constituent elements have relatively unchanged concentrations in the substrate and the  
18  
19 coating. An interfacial zone of approximately 6 nm, containing all four elements Fe, Cr, O  
20  
21 and Si is detected. The concentrations of Fe and Cr in the interface decrease from the  
22  
23 substrate towards the coating and those of O and Si increase.  
24  
25

26  
27 The energy-loss near-edge fine-structure (ELNES) in EELS is a powerful tool in probing the  
28  
29 local chemistry of a sample, containing information such as chemical bonding, oxidation  
30  
31 state, crystal structure and coordination<sup>38</sup>. EEL spectra recorded at different points along the  
32  
33 interface are plotted in Figure 2(a) (O, Cr, Fe) and Figure 2(b) (Si). Here we analyze the  
34  
35 ELNES of the spectra in different regions:  
36  
37

38  
39 **Coating.** The signal acquired in the coating contains the Si L- and the O K-edges. The  
40  
41 ELNES in both the Si L<sub>2,3</sub>- and O K-edges in this region (spectra at position (i)) resemble  
42  
43 closely those for amorphous SiO<sub>2</sub> with SiO<sub>4</sub> tetrahedral networks<sup>39-41</sup>: the Si L<sub>2,3</sub>-edge  
44  
45 contains three main peaks at ~ 106 eV, ~ 108 eV and ~ 115 eV. The first peak corresponds to  
46  
47 2p to unoccupied s-type states in Si and its onset has been shown to vary from ~ 100 eV for  
48  
49 Si<sup>0</sup> to ~ 103 eV for Si<sup>2+</sup> to ~ 105 eV for Si<sup>4+</sup><sup>42</sup>. The peaks at 108 eV and 115 eV arise from 2p  
50  
51 to dominantly d-type states, and are influenced by the Si – O tetrahedral coordination in  
52  
53 silica<sup>39,40</sup>. The O K-edge in the coating features a main peak at ~ 537 eV and a broad peak at ~  
54  
55 560 eV.  
56  
57

1  
2  
3 **Interface.** The spectra acquired in the interface contains signals from Si, O, Cr and Fe. Little  
4 change is observed in the fine structure of Si L<sub>2,3</sub>-edge at position (ii) in the interface relative  
5 to the coating. This indicates the continued dominant presence of [SiO<sub>4</sub>]<sup>4-</sup> units in the  
6 interface. The splitting in the initial peak at 106 eV, due to spin-orbit coupling of 2p electrons  
7 in Si, can be clearly resolved here<sup>41,43</sup>. A pre-peak at ~ 103 eV appears in the spectra at  
8 positions (iii) and (iv). The reduced onset energy of the Si L<sub>2,3</sub> edge signifies a lower  
9 oxidation number of Si at these positions, which may be related to the presence of Fe and Cr  
10 in the interface, *e.g.* due to the formation of olivine (Me<sub>2</sub>SiO<sub>4</sub>)-structure phases such as  
11 Fe<sub>2</sub>SiO<sub>4</sub><sup>39</sup> or Cr-bearing Si sub-oxides<sup>40</sup>. The O K-edges from positions (ii) and (iii) have  
12 overall similar profiles to that acquired in the coating. The first peak at ~ 537 eV arises  
13 mainly from scattering of excited electrons (from 1s state in O) by second nearest O neighbors  
14 and beyond<sup>44</sup> and has been shown to have little dependence on *e.g.* the Si – O – Si bond  
15 angle<sup>45,46</sup>. The peak at ~ 560 eV has been shown to shift to lower energies with increasing Si –  
16 O bond length (*i.e.* reduced ionic character)<sup>44</sup>. Such a shift is observed in the O K-edge at  
17 position (ii) and (iii). Additionally, the peak at ~ 537 eV in the spectra acquired at positions  
18 (ii), (iii) and (iv) contains a shoulder on the right hand side, indicating a larger crystal field  
19 effect<sup>47</sup> compared to position (i). This could be the result of distortion or change in the  
20 structure of the interface relative to the coating. A decrease in the onset energy of the O K-  
21 edge and a hint of a pre-peak can be seen in the spectra at positions (iii) and (iv). A pre-peak  
22 is typically present in the ELNES of the O K-edge of transition metal oxides<sup>48,49</sup> and a similar  
23 decrease in onset energy of the O K-edge can be observed for silicates such as Fe<sub>2</sub>SiO<sub>4</sub>  
24 (fayalite)<sup>50</sup>. The L<sub>2,3</sub> edges of transition metals reveal valuable information regarding their  
25 oxidation state, crystal structure and chemical environment. For example, the position of the  
26 L<sub>2</sub> and L<sub>3</sub> peaks are shown to be sensitive to their oxidation and shift typically to higher  
27 energies with increasing oxidation state<sup>49,51–54</sup>. The intensity ratio of L<sub>3</sub>/L<sub>2</sub> edges in transition  
28 metals is another important parameter related to the d-orbital occupancy (and subsequently  
29  
30  
31  
32  
33  
34  
35  
36  
37  
38  
39  
40  
41  
42  
43  
44  
45  
46  
47  
48  
49  
50  
51  
52  
53  
54  
55  
56  
57  
58  
59  
60

1  
2  
3 the oxidation state). Each of the  $L_2$  and  $L_3$  peaks can also contain fine details, stemming from  
4  
5 crystal field effects, which provide further clues to the chemical state of the transition  
6  
7 metal<sup>49,51,54</sup>. The peak maxima of the Fe  $L_3$  and  $L_2$  here are positioned respectively at  $\sim 707$   
8  
9 eV and  $\sim 720$  eV, without showing any noticeable change across the interface (see spectra (ii)  
10  
11 – (iv)). The average integrated intensity of  $L_3/L_2$  edges of Fe in the interface region  
12  
13 determined according to the method described by van Aken *et al.*<sup>47</sup> is 3.5 ( $L_3/L_2$  ratio in the  
14  
15 substrate is  $\sim 2.8$ ). Both the peak maxima energies and the  $L_3/L_2$  ratio in the interface region  
16  
17 correspond well to those for  $Fe^{2+}$ <sup>47,49,51,55</sup>. The fine structure present on the Fe  $L_{2,3}$  edge  
18  
19 across the interface is also consistent with this observation: A splitting in the  $L_3$  edge (marked  
20  
21 with arrows in spectra (ii) and (iii) of Fe  $L_{2,3}$  edges in Figure 2(a)) can be resolved,  
22  
23 characterized by a small bump at  $\sim 710$  eV after the main peak<sup>47,49,51</sup>. We thus conclude that  
24  
25 the Fe present in the interface region is predominantly in  $Fe^{2+}$  state. In the case of Cr, small  
26  
27 shifts in the  $L_3$  peak maxima at different points across the interface are detected. The  
28  
29 measured  $L_3$  and  $L_2$  peak maxima at position (iii) of  $\sim 576$  eV and  $\sim 585$  eV correspond  
30  
31 closely to  $Cr^{2+}$ <sup>52,54</sup>. Although the fine structure on the Cr  $L_3$  edge cannot be clearly resolved  
32  
33 in our measurements, its overall profile at position (iii) also suggests the presence of  $Cr^{2+}$ <sup>52,54</sup>.  
34  
35 In comparison, the Cr  $L_3$  peaks at positions (ii) and (iv) have their maxima at slightly higher  
36  
37 energies (approximately 1.0 eV and 0.6 eV shifts at positions (ii) and (iv), respectively). Their  
38  
39 overall shapes also varies compared to the Cr  $L_{2,3}$  edge at position (iii): this is in particular  
40  
41 clear at position (ii), where Cr  $L_3$  has a longer tail to the left of its main peak, suggesting that  
42  
43  $Cr^{3+}$  may also be present<sup>52,54</sup>.  
44  
45  
46  
47  
48

49 **Substrate.** The spectra collected from the substrate contain signals from Fe and Cr in metallic  
50  
51 form.  
52  
53

54 A reasonable hypothesis based on the results of our ELNES analysis of the interface is that it  
55  
56 is composed of  $Fe_2SiO_4$ ,  $Cr_2SiO_4$  and small amounts of  $Cr^{3+}$ -rich oxides such as  $Cr_2O_3$  or  
57  
58  
59  
60

1  
2  
3  $\text{Cr}^{3+}$ -bearing spinel, which have previously been reported as high temperature oxides of CrNi  
4 steels<sup>56</sup>. High-resolution TEM (HRTEM) images of the structure reveals that the interface is  
5 crystalline (see also Figure S1 in the supporting information (SI)). A HRTEM image of the  
6 substrate – coating structure with fast Fourier transform (FFT) patterns corresponding to  
7 regions within each of the substrate, interface and the coating are depicted in Figure 3. The  
8 crystalline nature of the substrate and the interface can be clearly seen in the image. However,  
9 the FFT patterns obtained from the substrate and the interface regions are distinctly different,  
10 indicating that the two regions have different crystal structures. Although not in a low-index  
11 zone-axis orientation, the FFT pattern of the interface is compatible with a  $\text{Fe}_2\text{SiO}_4$  structure  
12 (see Figure S2 in the SI).  
13  
14  
15  
16  
17  
18  
19  
20  
21  
22  
23

24 The interface formation is expected to resemble the thermal oxidation of the substrate at low  
25 oxygen partial pressure ( $\text{O}_2$  pp.) and elevated Si-access, whereby the  $\text{O}_2$  pp. is expected to  
26 show a decrease from the outer region of the interface (e.g. position (ii) in Figure 2) to its  
27 inner region (e.g. position (iv) in Figure 2). Thus, the interface formation has been simulated  
28 by computation of the phase equilibrium of the substrate composition vs.  $\text{O}_2$  pp. at 600 °C at  
29 elevated Si-level (for the computation a Si content of 2 wt.% has been assumed). The  
30 respective property diagram showing the phase equilibrium is shown in Figure 4. Clearly, the  
31 oxide-phase equilibrium is dominated by a Fe/Cr/Ni/Mn-rich spinel-structure oxide ( $\text{M}_3\text{O}_4$ ),  
32 together with an Fe/Cr-rich corundum-structure oxide ( $\text{M}_2\text{O}_3$ ) at high  $\text{O}_2$  pp. and a  
33 stoichiometric  $\text{Cr}_2\text{O}_3$  (corundum-structure) at low  $\text{O}_2$  pp., which generally agrees with the  
34 medium temperature oxides that have been experimentally identified after the oxidation of  
35 CrNi steel<sup>56</sup>. Neither of the previously discussed phases is enriched in Si. Si is entirely bound  
36 in form of quartz ( $\text{SiO}_2$ ) over a broad range of  $\text{O}_2$  pp. or a Fe-rich olivine-structure phase at  
37 medium  $\text{O}_2$  pp. (i.e. fayalite). Overall, the equilibrium calculation supports the hypothesis of  
38 fayalite formation in the interfacial zone together with the formation of  $\text{Cr}_2\text{O}_3$  directly at the  
39 substrate surface, where the lowest  $\text{O}_2$  pp. is expected. Further, the calculated phase  
40  
41  
42  
43  
44  
45  
46  
47  
48  
49  
50  
51  
52  
53  
54  
55  
56  
57  
58  
59  
60

1  
2  
3 equilibrium is in agreement with the observation of  $\text{Cr}^{3+}$  in the outer region of the interfacial  
4 zone, which may be bound in a spinel-type oxide where the highest  $\text{O}_2$  pp. is expected. Since  
5 no trace of  $\text{Fe}^{3+}$  was evident from the experiment, we propose that the formation of an outer  
6 corundum-structure layer was suppressed by the low oxygen availability during the thermal  
7 treatment. The formation of a thin, chemically bonded interfacial zone has been previously  
8 linked to good adhesion between glasses and metals<sup>35,40</sup>. Hence, the herein presented  
9 formation of a silicate-rich interaction zone may be directly linked to the adhesion of the  
10 coating, and thus prevent coating spallation and ensure an excellent performance and  
11 mechanical durability of SOG based coatings in industrial applications<sup>57</sup>. Further, the  
12 formation of a silicate-rich interface zone has been related to an increased corrosion  
13 resistance<sup>11</sup>, and thus the herein observed interfacial zone may have a strong positive impact  
14 on the corrosion behavior of the coating system. A detailed study of the performance of SOG  
15 coatings on stainless steel substrates including a discussion of the impact of the herein  
16 reported interface layer will be the content of following investigations.

#### 34 35 **4 Summary and Conclusions**

36  
37 In summary, we investigated the chemistry of the interface between AISI 316L and SOG  
38 coating using STEM-EELS and HRTEM imaging. An interfacial region of  $\sim 10$  nm thickness,  
39 containing Si, O, Cr and Fe was detected. Analysis of the ELNES indicated these elements to  
40 be in  $\text{Fe}^{2+}$ ,  $\text{Cr}^{2+}$  (as well as, small amounts of  $\text{Cr}^{3+}$ ) and  $[\text{SiO}_4]^{4-}$  forms. HRTEM images of the  
41 structure reveals that the interface is crystalline, with the FFT patterns matching a  $\text{Fe}_2\text{SiO}_4$   
42 (fayalite) -structure. The experimental results have been validated by thermodynamics  
43 simulations and we suggest that thermal processing of the SOG leads to the formation of a  
44 chemical interaction zone with the substrate which may generate excellent adhesion of the  
45 coating.

## Acknowledgements

This work is funded by Innovation Fund Denmark under grant number 50-2014-1. The authors acknowledge SiOx Aps, Denmark, for the deposition of the coatings and all other project partners. The A. P. Møller and Chastine Mc-Kinney Møller Foundation is gratefully acknowledged for their contribution toward the establishment of the Centre for Electron Nanoscopy at the Technical University of Denmark.

## References

- (1) Garzino-Demo, G. A.; Lama, F. L. Friction and Wear of Uncoated or SiO<sub>2</sub>-Coated 329 Stainless Steel and of Uncoated or AlN-Coated Aluminium Surfaces. *Surf. Coatings Technol.* **1994**, *68/69*, 507–511.
- (2) Gallardo, J.; Duran, A.; Garcia, I.; Celis, J. P.; Arenas, M. A.; Conde, A. Effect of Sintering Temperature on the Corrosion and Wear Behavior of Protective SiO<sub>2</sub>-Based Sol-Gel Coatings. *J. Sol-Gel Sci. Technol.* **2003**, *27*, 175–183.
- (3) Walke, W.; Paszenda, Z.; Basiaga, M.; Karasinski, P.; Kaczmarek, M. EIS Study of SiO<sub>2</sub> Oxide Film on 316L Stainless Steel for Cardiac Implants. In *Information Technologies in Biomedicine, Vol 4*; Piętka, E., Kawa, J., Wieclawek, W., Eds.; Advances in Intelligent Systems and Computing; Springer International Publishing: Cham, 2014; Vol. 283, pp 403–410.
- (4) Walke, W.; Paszenda, Z.; Pustelny, T.; Opilski, Z.; Drewniak, S.; Ko, M.; Basiaga, M. Evaluation of Physicochemical Properties of SiO<sub>2</sub>-Coated Stainless Steel after Sterilization. *Mater. Sci. Eng. C* **2016**, *63*, 155–163.
- (5) Santos, O.; Nylander, T.; Rosmaninho, R.; Rizzo, G.; Yiantsios, S.; Andritsos, N.; Karabelas, A.; Müller-Steinhagen, H.; Melo, L.; Boulangé-Petermann, L.; et al. Modified Stainless Steel Surfaces Targeted to Reduce Fouling—surface

- 1  
2  
3 Characterization. *J. Food Eng.* **2004**, *64* (1), 63–79.  
4  
5  
6 (6) Rosmaninho, R.; Santos, O.; Nylander, T.; Paulsson, M.; Beuf, M.; Benezech, T.;  
7 Yiantsios, S.; Andritsos, N.; Karabelas, A.; Rizzo, G.; et al. Modified Stainless Steel  
8 Surfaces Targeted to Reduce Fouling – Evaluation of Fouling by Milk Components. *J.*  
9  
10 Surfaces Targeted to Reduce Fouling – Evaluation of Fouling by Milk Components. *J.*  
11 *Food Eng.* **2007**, *80* (4), 1176–1187.  
12  
13  
14 (7) Mohaghegh, K.; Hansen, H. N.; Pranov, H.; Kofod, G. A Study on the Surface  
15 Roughness of a Thin HSQ Coating on a Fine Milled Surface. In *14th euspen*  
16 *International Conference - Dubrovnik*; 2014.  
17  
18  
19 (8) Mohaghegh, K.; Hansen, H. N.; Pranov, H.; Kofod, G. Verification of Thickness and  
20 Surface Roughness of a Thin Film Transparent Coating. In *Proceedings of the 13th*  
21 *euspen International Conference*; Berlin, 2013.  
22  
23  
24 (9) Cech, J.; Pranov, H.; Kofod, G.; Matschuk, M.; Murthy, S.; Taboryski, R. Surface  
25 Roughness Reduction Using Spray-Coated Hydrogen Silsesquioxane Reflow. *Appl.*  
26 *Surf. Sci.* **2013**, *280*, 424–430.  
27  
28  
29 (10) Hobæk, T. C.; Matschuk, M.; Kafka, J.; Pranov, H. J.; Larsen, N. B. Hydrogen  
30 Silsesquioxane Mold Coatings for Improved Replication of Nanopatterns by Injection  
31 Molding. *J. Micromechanics Microengineering* **2015**, *25* (3), 035018 (9pp).  
32  
33  
34 (11) Vasconcelos, D. C. L.; Carvalho, J. A. N.; Mantel, M.; Vasconcelos, W. L. Corrosion  
35 Resistance of Stainless Steel Coated with Sol–gel Silica. *J. Non. Cryst. Solids* **2000**,  
36 *273* (1–3), 135–139.  
37  
38  
39 (12) Hwang, T.; Lee, H.; Kim, H.; Kim, G. Two Layered Silica Protective Film Made by a  
40 Spray-and-Dip Coating Method on 304 Stainless Steel. *J. Sol-Gel Sci. Technol.* **2010**,  
41 *55* (2), 207–212.  
42  
43  
44 (13) Pech, D.; Steyer, P.; Millet, J.-P. Electrochemical Behaviour Enhancement of Stainless  
45  
46  
47  
48  
49  
50  
51  
52  
53  
54  
55  
56  
57  
58  
59  
60

- 1  
2  
3 Steels by a SiO<sub>2</sub> PACVD Coating. *Corros. Sci.* **2008**, *50* (5), 1492–1497.
- 4  
5 (14) Atik, M.; de Lima Neto, P.; Avaca, L. A.; Aegerter, M. A.; Zarzycki, J. Protection of  
6  
7 316L Stainless Steel against Corrosion by SiO<sub>2</sub> Coatings. *J. Mater. Sci. Lett.* **1994**, *13*  
8  
9 (15), 1081–1085.
- 10  
11 (15) de Sanctis, O.; Gomez, L.; Pellegrini, N.; Parodi, C.; Marajofsky, A.; Duran, A.  
12  
13 Protective Glass Coatings on Metallic Substrates. *J. Non. Cryst. Solids* **1990**, *121*, 338–  
14  
15 343.
- 16  
17 (16) de Sanctis, O.; Gomez, L.; Pellegrini, N.; Duran, A. Behaviour in Hot Ammonia  
18  
19 Atmosphere of SiO<sub>2</sub>-Coated Stainless Steels Produced by a Sol-Gel Procedure. *Surf.*  
20  
21 *Coatings Technol.* **1995**, *70*, 251–255.
- 22  
23 (17) Foggiano, J. Chemical Vapor Deposition of Silicon Dioxide Films. In *Handbook of*  
24  
25 *Thin Film Deposition Processes and Techniques (Second Edition)*; Elsevier B.V.,  
26  
27 2001; pp 111–149.
- 28  
29 (18) Møller, P.; Nielsen, L. P. Physical Vapor Deposition. In *Advanced Surface Technology,*  
30  
31 *Vol 1*; 2013; pp 457–482.
- 32  
33 (19) Brinker, C. J.; Scherer, G. W. Hydrolysis and Condensation of Silicon Alkoxides. In  
34  
35 *Sol-Gel Science*; Academic Press, Inc.: San Diego, 1990; pp 108–216.
- 36  
37 (20) Nagayama, H.; Honda, H.; Kawahara, H. A New Process for Silica Coating. *J.*  
38  
39 *Electrochem. Soc.* **1988**, *135* (8), 2013–2016.
- 40  
41 (21) Többen, D.; Weigand, P.; Shapiro, M. J.; Cohen, S. A. Influence of the Cure Process on  
42  
43 the Properties of Hydrogen Silsesquioxane Spin-on-Glass. *Mater. Res. Soc. Symposium*  
44  
45 *Proc.* **1997**, *443*, 195–200.
- 46  
47 (22) Loboda, M. J.; Grove, C. M.; Schneider, R. F. Properties of a-SiO<sub>x</sub>:H Thin Films  
48  
49 Deposited from Hydrogen Silsesquioxane Resins. *J. Electrochem. Soc.* **1998**, *145* (8),  
50  
51  
52  
53  
54  
55  
56  
57  
58  
59  
60



- 1  
2  
3 2861–2866.  
4  
5 (23) Siew, Y. K.; Sarkar, G.; Hu, X.; Hui, J.; See, A.; Chua, C. T. Thermal Curing of  
6 Hydrogen Silsesquioxane. *J. Electrochem. Soc.* **2000**, *147* (1), 335.  
7  
8  
9  
10 (24) Bremmer, J. N.; Liu, Y.; Gruszynski, K. G.; Dall, F. C. Cure of Hydrogen  
11 Silsesquioxane for Intermetal Dielectric Applications. *Mater. Res. Soc. Symp. Proc.*  
12 **1997**, *476*, 37–44.  
13  
14  
15  
16  
17 (25) Choi, S. K. Nanolithography and Nanofabrication Using Hydrogen Silsesquioxane  
18 Resists (Dissertation), University of Illinois, 2009.  
19  
20  
21 (26) Lampert, F.; Jensen, A. H.; Din, R. U.; Møller, P. Hydrogen Silsesquioxane Based  
22 Silica Glass Coatings for the Corrosion Protection of Austenitic Stainless Steel. *Surf.*  
23 *Coatings Technol.* **2016**, *307*, 879–885.  
24  
25  
26  
27  
28 (27) Lampert, F.; Kadkhodazadeh, S.; Jensen, A. H.; Din, R. U.; Møller, P. Interfacial  
29 Interaction of Oxidatively Cured Hydrogen Silsesquioxane Spin-On-Glass Enamel with  
30 Stainless Steel Substrate. *J. Electrochem. Soc.* **2017**, *164* (6), C231–C239.  
31  
32  
33  
34  
35 (28) Lampert, F.; Christiansen, A. B.; Din, R. U.; Gonzalez-Garcia, Y.; Møller, P. Corrosion  
36 Resistance of AISI 316L Coated with an Air-Cured Hydrogen Silsesquioxane Based  
37 Spin-On-Glass Enamel in Chloride Environment. *Corros. Sci.* **2017**, *127*, 110–119.  
38  
39  
40  
41  
42 (29) ASTM Standard A480/A480M 14b: Standard Specification for General Requirements  
43 for Flat-Rolled Stainless and Heat-Resisting Steel Plate, Sheet, and Strip. ASTM  
44 International: West Conshohocken 2016, pp 1–26.  
45  
46  
47  
48  
49 (30) Shieu, F. S.; Deng, M. J.; Lin, K. C.; Wong, J. C.; Wu, J. Y. Effect of Surface  
50 Pretreatments on the Adherence of Porcelain Enamel to a Type 316L Stainless Steel. *J.*  
51 *Mater. Sci.* **1999**, *34*, 5265–5272.  
52  
53  
54  
55  
56 (31) Stoch, A.; Stoch, J.; Rakowska, A. An XPS and SEMS Study of Silica Sol-Gel/metal  
57  
58  
59  
60

- 1  
2  
3 Substrate Interaction. *Surf. Interface Anal.* **1994**, *22*, 242–247.  
4  
5  
6 (32) Takemori, M. Crack Formation, Exfoliation, and Ridge Formation in 500 °C Annealed  
7 Sol-Gel Silica Coatings on Stainless Steel SUS304: Part I. Microscopic Observations  
8 and Elemental Analysis. *Ceram. Int.* **2009**, *35*, 1731–1746.  
9  
10  
11  
12 (33) Takemori, M. Crack Formation, Exfoliation, and Ridge Formation in 500 °C Annealed  
13 Sol-gel Silica Coatings on Stainless Steel SUS304: Part II Spectroscopic and  
14 Mechanical Analyses and Insights into Mechanisms Controlling Coating  
15 Characteristics. *Ceram. Int.* **2009**, *35* (5), 1747–1755.  
16  
17  
18  
19  
20  
21 (34) Onyiriuka, E. C.; Kinney, L. D.; Binkowski, N. J. Adhesion and Delamination of  
22 Tantalum and Chromium Films on Glass. *J. Adhes. Sci. Technol.* **1997**, *11* (7), 929–  
23 940.  
24  
25  
26  
27  
28 (35) Benjamin, P.; Weaver, C. The Adhesion of Evaporated Metal Films on Glass. *Proc. R.*  
29 *Soc. London. Ser. A, Math. Phys.* **1961**, *261* (1307), 516–531.  
30  
31  
32  
33 (36) Peuker, M.; Lim, M. H.; Smith, H. I.; Morton, R.; van Langen-Suurling, A. K.; Romijn,  
34 J.; van der Drift, E. W. J. M.; van Delft, F. C. M. J. M. Hydrogen SilsesQuioxane, a  
35 High-Resolution Negative Tone E-Beam Resist, Investigated for Its Applicability in  
36 Photon-Based Lithographies. *Microelectron. Eng.* **2002**, *61–62*, 803–809.  
37  
38  
39  
40  
41  
42 (37) Andersson, J. O.; Helander, T.; Höglund, L.; Shi, P. F.; Sundman, B. Thermo-Calc and  
43 DICTRA, Computational Tools for Materials Science. *Calphad* **2002**, *26*, 273–312.  
44  
45  
46  
47 (38) Keast, V. J.; Bruley, J. Electron Energy-Loss near-Edge Structure - a Tool for the  
48 Investigation of Electronic Structure on the Nanometre Scale. *J. Microsc.* **2001**, *203*  
49 (August), 135–175.  
50  
51  
52  
53 (39) Garvie, L. A. G.; Useck, P. R. Bonding in Silicates : Investigation of the Si L 2 , 3  
54 Edge by Parallel Electron Energy-Loss Spectroscopy. *Am. Mineral.* **1999**, *84*, 946–964.  
55  
56  
57

- 1  
2  
3 (40) Jiang, N.; Silcox, J.; Jiang, N.; Silcox, J. Observations of Reaction Zones at Chromium  
4 / Oxide Glass Interfaces. *J. Appl. Phys.* **2000**, *87* (8), 3768.  
5  
6  
7 (41) Batson, P. E. Atomic Resolution Electronic Structure in Silicon-Based  
8 Semiconductors. *J. Electron Microsc. (Tokyo)*. **1996**, *45* (1), 51–58.  
9  
10  
11 (42) Batson, P. E. Simultaneous STEM Imaging and Electron Energy-Loss Spectroscopy  
12 with Atomic-Column Sensitivity. *Nature* **1993**, *366*, 727–728.  
13  
14  
15 (43) Krivanek, O. L.; Lovejoy, T. C.; Dellby, N.; Carpenter, R. W. Monochromated STEM  
16 with a 30 meV-Wide , Atom-Sized Electron Probe. *Microscopy* **2013**, *62* (1), 3–21.  
17  
18  
19 (44) Wallis, D. J.; Gaskell, P. H.; Brydson, R. Oxygen K near-Edge Spectra of Amorphous  
20 Silicon Suboxides. *J. Microsc.* **1986**, *180* (3), 307–312.  
21  
22  
23 (45) Davoli, I.; Paris, E.; Stizza, E.; Benfatto, S.; Fanfoni, M.; Gargano, M.; Bianconi, A.;  
24 Seifert, F. Structure of Densified Vitreous Silica : Silicon and Oxygen XANES Spectra  
25 and Multiple Scattering Calculations. *Phys. Chem. Miner.* **1992**, *19* (3), 171–175.  
26  
27  
28 (46) Brown, G. E.; Waychunas, G. A.; Stohr, J.; Sette, F. Near-Edge Structure of Oxygen in  
29 Inorganic Oxides: Effect of Local Geometry and Cation Type. *Le J. Phys. Colloq.*  
30 **1986**, *47* (C8), C8-685-C8-689.  
31  
32  
33 (47) van Aken, P. A.; Liebscher, B. Quantification of Ferrous / Ferric Ratios in Minerals :  
34 New Evaluation Schemes of Fe L 23 Electron Energy-Loss near-Edge Spectra. *Phys.*  
35 *Chem. Miner.* **2002**, *29*, 188–200.  
36  
37  
38 (48) Krivanek, O. L.; Paterson, J. H. ELNES of Transition Metal Oxides I. Variations across  
39 the Periodic Table. *Ultramicroscopy* **1990**, *32*, 313–318.  
40  
41  
42 (49) Paterson, J. H.; Krivanek, O. L. ELNES OF 3d TRANSITION-METAL OXIDES 2.  
43 Variations with Oxidation State and Crystal Structure. *Ultramicroscopy* **1990**, *32*, 319–  
44 325.  
45  
46  
47  
48  
49  
50  
51  
52  
53  
54  
55  
56  
57  
58  
59  
60

- 1  
2  
3 (50) Garvie, L. A. G. Can Electron Energy-Loss Spectroscopy (EELS) Be Used to Quantify  
4 Hydrogen in Minerals from the O K Edge? *Am. Mineral.* **2010**, *95*, 92–97.  
5  
6  
7 (51) Tan, H.; Verbeeck, J.; Abakumov, A.; Van Tendeloo, G. Oxidation State and Chemical  
8 Shift Investigation in Transition Metal Oxides by EELS. *Ultramicroscopy* **2012**, *116*,  
9 24–33.  
10  
11  
12  
13  
14 (52) Arévalo-López, A. M.; Alario-Franco, M. A. Reliable Method for Determining the  
15 Oxidation State in Chromium Oxides. *Inorg. Chem.* **2009**, *48* (24), 11843–11846.  
16  
17  
18  
19 (53) Malinsky, M. D.; Kelly, K. L.; Schatz, G. C.; Van Duyne, R. P. Nanosphere  
20 Lithography: Effect of Substrate on the Localized Surface Plasmon Resonance  
21 Spectrum of Silver Nanoparticles. *J. Phys. Chem. B* **2001**, *105*, 2343–2350.  
22  
23  
24  
25  
26 (54) Stoyanov, E.; Langenhorst, F. The Effect of Valence State and Site Geometry on Cr  
27 L<sub>3,2</sub> Electron Energy-Loss Spectra of Cr-Bearing Oxidic Compounds. *Chemie der*  
28 *Erde - Geochemistry* **2014**, *74* (3), 497–505.  
29  
30  
31  
32  
33 (55) de Groot, F. M. F.; Fuggle, J. C.; Thole, B. T.; Sawatzky, G. A. 2p X-Ray Absorption  
34 of 3d Transition-Metal Compounds: An Atomic Multiplet Description Including the  
35 Crystal Field. *Phys. Rev. B* **1990**, *42* (9), 5459–5468.  
36  
37  
38  
39  
40 (56) Lussana, D.; Baldissin, D.; Massazza, M.; Baricco, M. Thermodynamic and Kinetics  
41 Aspects of High Temperature Oxidation on a 304L Stainless Steel. *Oxid. Met.* **2014**, *81*  
42 (5–6), 515–528.  
43  
44  
45  
46  
47 (57) Lee, G. H.; Cailler, M.; Constantinescu, C.; Kwon, S. C. Adhesion Studies of Radio-  
48 Frequency Sputtered SiO<sub>2</sub> Films on Ti, Stainless Steel, Ni and Inconel Substrates.  
49 Effects of Substrate Surface Ion Bombardment Etching. *J. Adhes. Sci. Technol.* **1990**, *4*  
50 (6), 481–501.  
51  
52  
53  
54  
55  
56  
57

## Tables

**Table I:** Chemical composition of the substrates (by Optical Emission Spectroscopy). In addition, traces (< 0.1 wt.%; > 0.01 wt.%) of P, Nb, V, W were also detected.

<b>Element</b>	<b>Cr</b>	<b>Ni</b>	<b>Mo</b>	<b>Mn</b>	<b>Si</b>	<b>Cu</b>	<b>Co</b>	<b>N</b>	<b>C</b>	<b>Fe</b>
<b>Composition (wt.%)</b>	16.8	10.4	2.07	0.92	0.47	0.41	0.21	0.048	0.019	bal.

## Figure Captions

**Figure 1:** (a) HAADF STEM images of the coating on AISI 316L substrates in the cross-sectional geometry. (b) Relative composition profiles of O, Cr and Fe and the Si signal intensity across the interface extracted from EELS plotted together with the intensity profile of the HAADF STEM image along the line the EEL spectra were acquired from.

**Figure 2:** EELS spectra along a line across the coating – AISI 316L interface containing the (a) O K-, Cr L<sub>2,3</sub>- and Fe L<sub>2,3</sub>-edges and (b) Si L<sub>2,3</sub>-edge.

**Figure 3:** HRTEM image of the coating – AISI 316L interface, with FFT patterns of selected regions from the coating, interface and the substrate.

**Figure 4:** Phase equilibrium vs. O<sub>2</sub> partial pressure diagram of the substrate composition at increased (2 wt.%) Si-level. The property diagram was computed with Thermo-Calc Software version 2017a<sup>37</sup>, TCFE7.0.

## Figures

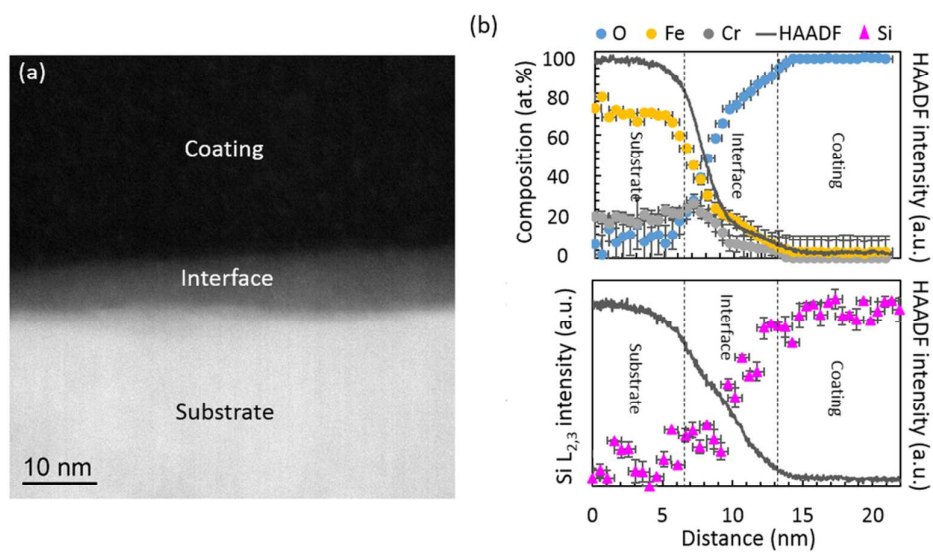


Figure 1

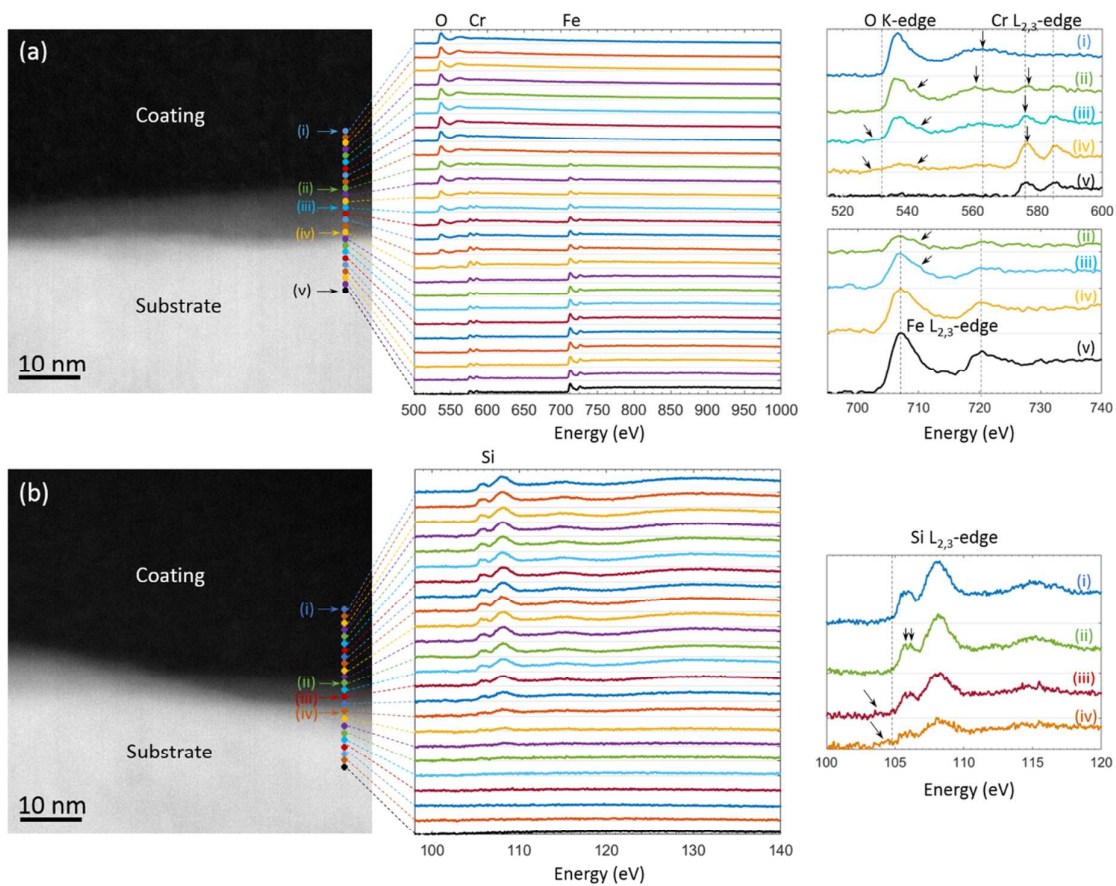
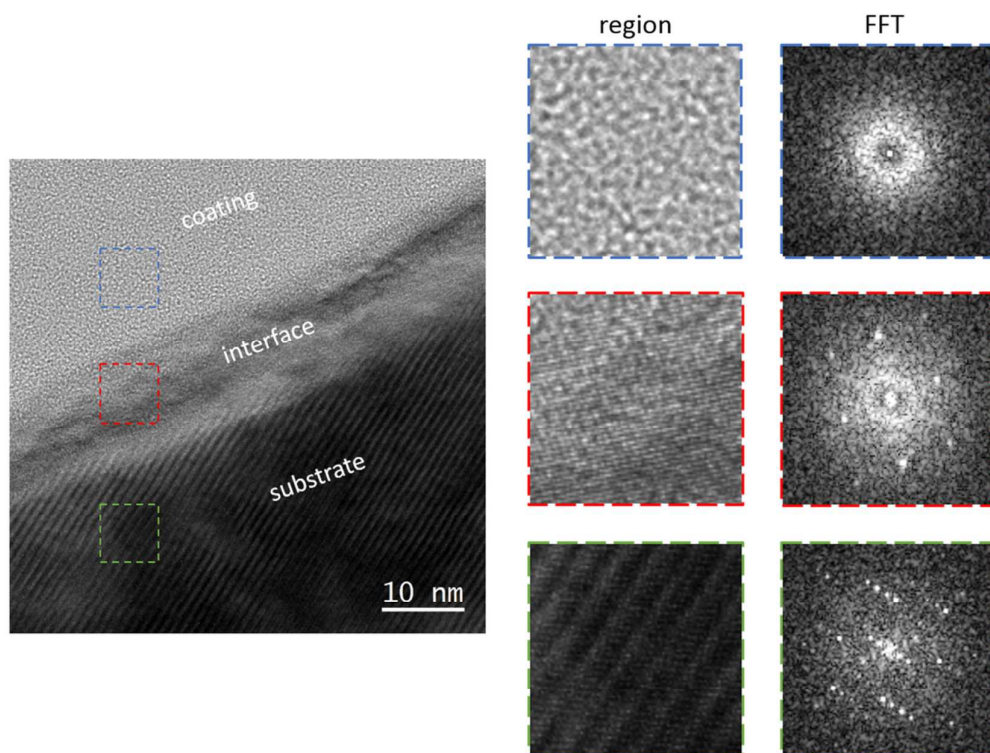


Figure 2





28  
29  
30  
31  
32  
33  
34  
35  
36  
37  
38  
39  
40  
41  
42  
43  
44  
45  
46  
47  
48  
49  
50  
51  
52  
53  
54  
55  
56  
57  
58  
59  
60

Figure 3

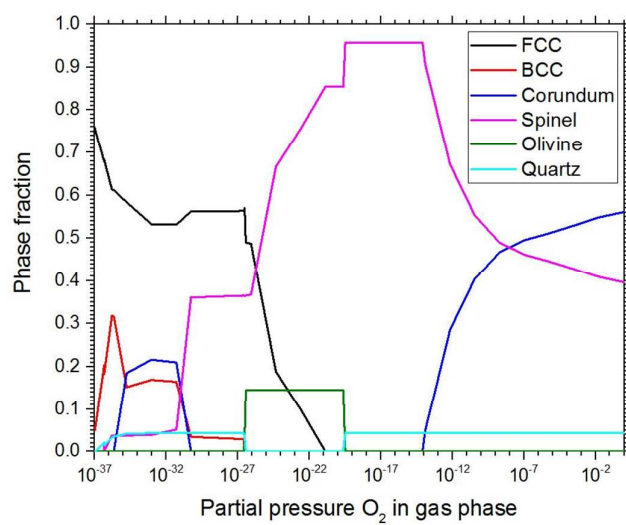


Figure 4